Balbiani Ring hnRNP Substructure Visualized by Selective Staining and Electron Spectroscopic Imaging

Ada L. Olins,* Donald E. Olins,* and David P. Bazett-Jones‡

*The University of Tennessee-Oak Ridge Graduate School of Biomedical Sciences, Biology Division, Oak Ridge, Tennessee 37831-8077, and ‡Department of Medical Biochemistry, The University of Calgary, Calgary, Alberta, Canada T2N 4N1

Abstract. The Balbiani Rings (BR) in the polytene chromosomes of Chironomus salivary glands are intense sites of transcription. The nascent RNPs fold during transcription into 40–50-nm granules, containing in the mature transcript ∼37-kb RNA. Using a new nucleic acid specific stain, osmium ammine B on Lowicryl sections, in combination with electron energy filtered imaging of sections containing BR granules, we demonstrate a RNA-rich particulate substructure (10-nm particle diameter; 10–12 particles per BR granule). Elemental imaging supports that these particles are enriched in phosphorus. The possible relationship of these RNA-rich particles to ribonucleosomes is discussed, as well as models for their arrangement in the mature BR granules.

NASCENT pre-mRNA transcribed by RNA polymerase II is rapidly packaged into repeating arrays of RNP particles (8, 9, 13, 14). These particles, variously named ribonucleosomes or heterogeneous nuclear ribonucleoprotein particles (hnRNP),[1] are composed of multiple copies of six major core proteins between 30–40 kD. When isolated nuclei are exposed briefly to RNase, the monomer hnRNPs are cleaved apart, resulting in the accumulation of particles that sediment at ∼40S. Reconstitution studies in vitro with purified core proteins and RNA substantiate the self assembly of the 40S hnRNP (1), composed of 700 nucleotides and stoichiometric amounts of proteins per monomer particle. Whereas nucleotide sequence does not seem to be important for the formation of hnRNP, assembly is highly dependent upon RNA length. Evolutionary conservation of core proteins has been demonstrated by antibody cross-reactivity and DNA hybridization across a broad range of organisms, including lower eukaryotes, insect, amphibia, avian and mammalian species (8).

The polytene chromosomes in the larval salivary glands of Chironomus insects exhibit regulated "puffs," known as Balbiani Rings (BR). Many of these BR are the sites of intense transcription of large mRNA molecules (7, 10). BR 1, 2, and 6 transcribe mRNAs that include species in the size range of 35–40 kb. The large protein products, denoted "sp-I" secretory proteins, are spun into a fibrous silk-like net that encloses the aquatic larvae and functions to trap food. BR hnRNPs are readily visualized by EM in stained sections of fixed salivary glands, appearing as 40–50-nm particles either connected via a stalk to the presumptive chromatin axis, or as mature granules within the nucleoplasm (6, 36). The packaging and arrangement of BR granules either attached to the chromatin axis, free within the nucleoplasm or traversing nuclear pores into the cytoplasm has been examined in numerous EM studies, using the methods of stereo-EM and electron microscope tomography (EMT) (19, 20, 22–26, 28, 33–35). These methods have led to the following conclusions: (a) At least in the case of the hyperactive pilocarpine-stimulated BR2 gene (23–26), the nascent transcripts are close packed along the chromatin axis at ∼80–100 granules/μm in an imperfect helical arrangement of five to seven granules/turn. The axis DNA is estimated to be compacted about threefold (whereas, a string of nucleosomes would be compacted seven- to eightfold), implying that the chromatin is markedly unfolded during the intense transcription; and (b) the outer diameter of the mature BR granule is ∼50 nm and appears to represent a coiled RNP ribbon of length, 120-nm long, 25–50-nm wide, 10–15-nm thick (33–35). As it passes through a nuclear pore, the BR granule unfolds into the RNP ribbon. Some observations suggest that the ribbon is composed of a 10-nm diam zigzag or spiral RNP filament (20). The BR hnRNP granules have been isolated and partially characterized (38, 39). These granules sediment at about 300S and consist of approximately 40% RNA and 60% protein. Treatment of isolated 300S BR granules with RNase A revealed some unexpected results. 40S ribonucleosomal particles were never observed. Most of the granules could sustain numerous nicks in the 37-kb RNA without a change in sedimentation. The authors (39) concluded that whether hnRNP particles exist within mature BR granules can not yet be answered. To better define the structural organization of the protein and nucleic acid components of BR granules, we combined a selective nucleic acid stain with EM.

---

1. *Abbreviations used in this paper:* BR, Balbiani Ring; EMT, electron microscope tomography; ESI, electron spectroscopic imaging; hnRNP, heterogeneous nuclear ribonucleoprotein; OA, osmium ammine.

The use of selective nucleic acid staining in EM offers the potential to visualize DNA- or RNA-containing structures without the additional electron density arising from stained proteins. The most successful approach in this direction has used the Schiff-like reagent, osmium ammine (OA) to stain DNA in sectioned nuclei after depurination and release of reactive aldehydes (12, 16). Because of the difficulty of reproducibly synthesizing usable preparations of OA, we (18, 27) developed a new more reliable synthesis procedure and final product denoted OA-B. As yet we do not know the detailed chemical composition of OA or OA-B, or whether they share any identical chemical components which are responsible for the stain specificity. A recent study (11) has demonstrated that, under suitable conditions, OA can give high resolution staining of both RNA and DNA. These conditions include: Lowicryl K4M embedding; no depurination, and staining with OA dissolved in 0.1 M glycine-HCl, pH 1.5, or SO_2-bubbled OA in water. Stain specificity was demonstrated by pretreatment of the sections with various nucleases and proteases. In the present study, we show that OA-B–treated Lowicryl sections produces a clear demonstration of an organized substructure within BR hnRNP particles.

One disadvantage with selective nucleic acid staining by OA or OA-B is the low inherent contrast of the fine osmium stain. These problems can be partially overcome by optimization of EM data collection by using a low-accelerating voltage, a small objective aperture and by photographic and digital enhancement. In this study, we optimize image contrast by collecting energy-filtered images of OA-B–stained sections. Electron spectroscopic imaging (ESI) is a relatively new method that uses an electron spectrometer situated below the specimen in a fixed beam EM, such as exists on the Zeiss EM902 microscope (Carl Zeiss, Inc., Oberkochen, Germany) (30). Within different regions of a section, electrons are inelastically scattered depending upon the chemical elements present within that region. It then becomes convenient to image selectively for a particular element by using the spectrometer to transmit a window of inelastically scattered electrons characteristic for that element. This method has been successfully used to image phosphorus within DNA and RNA containing structures (3–5, 29). Elemental imaging requires very thin sections to minimize multiple electron scattering events. In the present study, we used the spectrometer to enhance "structure-sensitive contrast" (2, 31) to minimize the contribution of carbon and strengthen the osmium signal in the final EM image. This was accomplished by imaging with electrons which have lost 250 eV, just before the carbon K edge ($\Delta E = 284$ eV) in the energy loss spectrum. When this method was combined with selective OA-B staining, the resulting darkfieldlike images revealed a discrete RNA-containing particulate substructure in the BR granules. Phosphorus mapping was also performed on BR granules present in very thin unstained sections, providing a strong indication that the particulate substructures are highly enriched in phosphorus.

Materials and Methods

Materials

Salivary glands from staged Chironomus tentans 4th instar larvae were fixed in 0.5% glutaraldehyde, 1.5% paraformaldehyde in PBS, pH 7.8, for 1 h, and then washed in PBS, and 0.05 M NH_4Cl, PBS, pH 7.5, before dehydration and embedding. The sequence of dehydration and embedding was as follows: 30 min, 30% EtOH, 0°C; 1 h, 50% EtOH, 0°C; 1 h, 70% EtOH, −35°C; 2 h, 100% EtOH, −35°C; 2 h, 1:1 EtOH:Lowicryl K4M, −35°C; 2 h, 1:2 EtOH: Lowicryl K4M, −35°C; overnight 100% Lowicryl K4M, −35°C; fresh Lowicryl K4M, −35°C was polymerized by reflected UV. The larvae had been stimulated 5 1/2 h with the smooth muscle contractant pilocarpine after awakening from prolonged oligopause. This protocol results in considerable stimulation of transcription of BR2, as detailed (17, 21). The salivary glands were fixed and washed in the laboratory of M. Lezzi (Zürich, Switzerland) and transported to the laboratory of E. Carlemalm and E. Kellenberger (Basel, Switzerland), where they were embedded at low temperature in the hydrophilic resin Lowicryl K4M. The fixation and embedding was performed in the space of several days in 1984. The blocks have been stored in a desiccator since then. Sections (75–150-nm thick) were prepared just before staining with OA-B. They were picked up on cleaned gold grids, without additional support.

Selective Staining with OA-B

OA-B prepared as described previously (18, 27), now available from Polysciences, Inc. (Warrington, PA) was used as described for OA (11). RNase and DNase pretreatment of sections followed the method described (11). Staining was performed with 0.2% OA-B in H_2O, bubbled with SO_2 for 20 min just before contact with the sections. Grids were immersed in the OA-B solution in capped Beem capsules and incubated at 37°C for 1 h. Stained grids were rinsed with water and air dried.

For EMT data collection, one microliter of 5-nm diam colloidal gold spheres (Energy Beam Sciences, Agawam, MA), diluted 1:100 in H_2O was adsorbed to each surface of the stained grids. The use of gold particle positions in alignment and registration of tilt images has been described previously (24, 35).

General Staining with Uranyl and Lead

Salivary glands were fixed in 3% glutaraldehyde, 50 mM Sorensen's buffer, pH 7.2, for 4 h, washed, and fixed in 1% OsO_4 in the same buffer, washed, dehydrated, and embedded in Epon. Sections were stained in 2% uranyl magnesium acetate for 20 min at 48°C and for 5 min in lead citrate.

Electron Spectroscopic Imaging (ESI)

Stained specimens were imaged on a Zeiss EM902 microscope equipped with a prism-mirror-prism type electron imaging spectrometer, top-entry tilt stage and an image-intensification video camera to permit data collection at reduced dose. The microscope was operated at an accelerating voltage of 80 kV. The width of the energy selecting slit aperture corresponds to 20eV. A 700 μm condenser and a 60 μm objective aperture were used. Because the tilt stage was not eucentric, the grid was rotated within the holder to bring a nucleus or BR2 onto the tilt axis, following a procedure outlined previously (28). This procedure was performed before collecting stereo pairs or a complete tilt series. Imaging was performed at $\Delta E = 250$ eV, before the carbon K edge at $\Delta E = 284$ eV. In some experiments the same field was photographed at selected energy losses to examine the change in contrast of the stained regions. Photographs were collected at 12, 20, 30, 50, and 85K magnification.

Phosphorus Mapping of BR Granules

Phosphorus distribution maps of BR granules were obtained using the methods described previously (3–5, 29). Two energy loss images of an unstained specimen were recorded, a pre-edge image at 120 eV and a phosphorus-enhanced image at 160 eV energy loss. Regions of interest on both micrographs were digitized and normalized to account for slight changes in exposure density over regions that were judged to be devoid of phosphorus. Alignment of the two digitized regions to within one pixel was accomplished by eye, by alternating the display between a stored phosphorus enhanced image and an on-line edge image being translated and rotated.

Subtraction of the aligned and normalized pre-edge image from the phosphorus enhanced image produces a net phosphorus image. We have previously shown that the results obtained with a one-parameter (one pre-edge image) and a two-parameter (two pre-edge images) are comparable, providing the specimen thickness is not greater than ~30 nm.
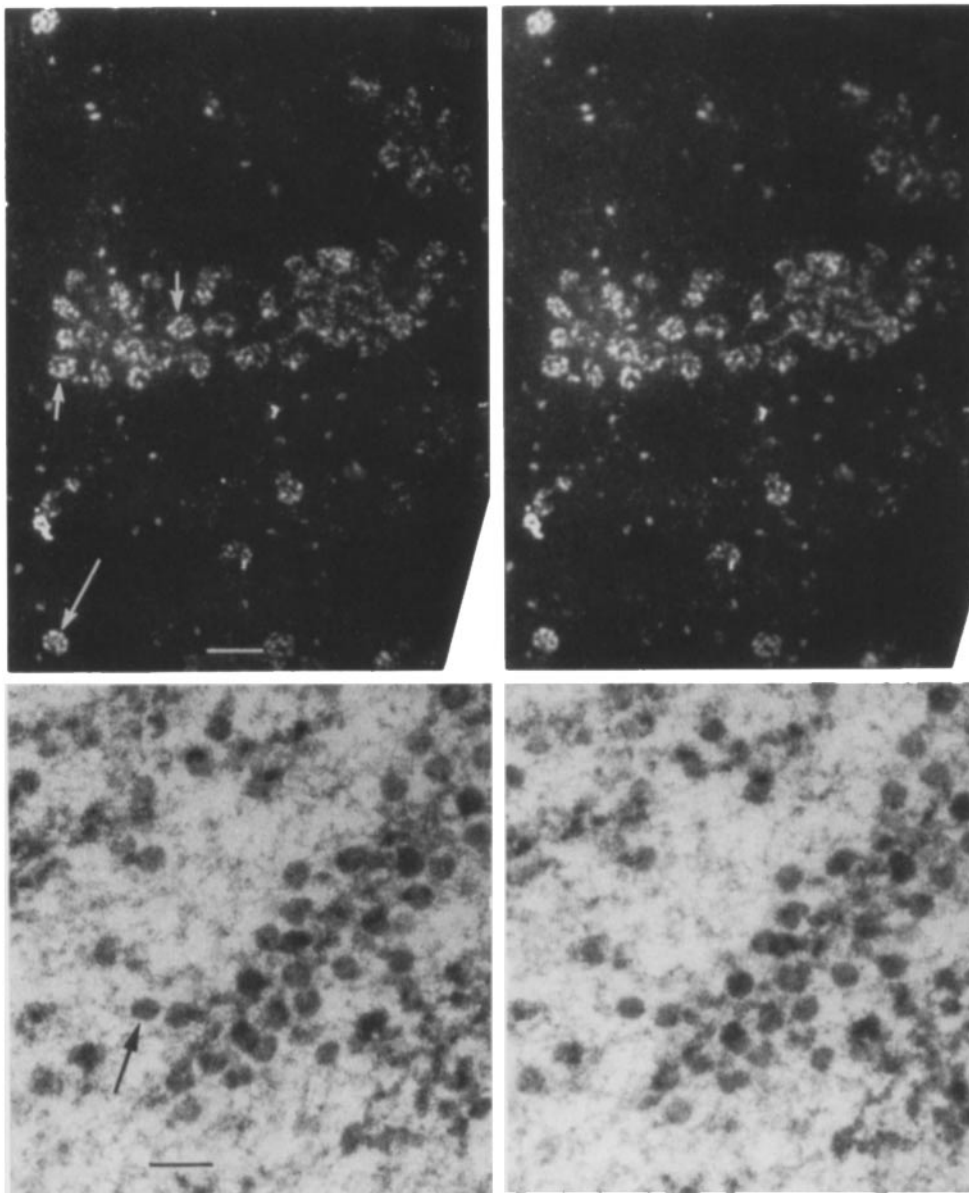
Figure 1. Two stereo EM pairs of similar nuclear regions including BR transcription axes containing attached nascent RNP granules and unattached mature BR granules within the nucleoplasm. The top pair was embedded in Lowicryl and stained with OA-B, under conditions which stain only nucleic acids and imaged using 250 ± 10 eV loss electrons. A portion of a transcription axis runs horizontally in the center of the field; attached nascent BR granules are indicated by the short arrows. A mature BR granule is indicated by the long arrow. The bottom stereo pair of a uranyl and lead stained salivary gland contains a portion of a transcription axis which traverses the field diagonally. This staining procedure contrasts both nucleic acid and protein, thus presenting a silhouette of mature (*long arrow*) and nascent BR granules. Bar, 100 nm.

Results

BR Granule Substructure

RNA and DNA are stained specifically with OA-B in Lowicryl sections as previously described for OA (11). In the giant cells of the Chironomus tentans salivary gland, RNA in ribosomes and in BR granules is clearly visible. In Fig. 1, stereo pairs of a BR transcription axis are shown: the upper panel is an image of a Lowicryl section stained with OA-B; the lower panel is a section stained with uranyl and lead (22, 23). In both panels, regions within the nucleus contain a cluster of nascent BR granules along a portion of the transcription axis and individual mature BR granules located throughout the nucleoplasm. Nascent and mature BR granules exhibit obvious particulate substructure after staining with OA-B. In Lowicryl sections pretreated with RNase, the contrast of RNPs is completely obliterated (Fig. 2 *E*), but DNA in the banded polytene chromosome (Fig. 2 *F*, lower half) retains high contrast. Prior treatment with DNase (not

shown) leaves the RNA staining but reduces the intensity of polytene chromosome bands only. The clarity of OA-B stained structures is striking. The stain is very fine, permitting detailed examination of specimens at high magnification.

Osmium Contrast Is Optimized Just below the Carbon K Edge

The same field of an OA-B–stained Lowicryl specimen was imaged with electrons of varying eV-loss (Fig. 2) in a manner analogous to a series of images previously published (31). Fig. 2, *A–D* presents several of these images. This field includes nucleoplasm (Fig. 2, *A–D*, bottom right), cytoplasm (top left) and nuclear envelope (approximately diagonal from top right to bottom left corners). Fig. 2 *A* presents a global bright-field image (elastically and inelastically scattered electrons). Ribosomes in the cytoplasm, gold particles, and hnRNP are darker than the background, but the contrast is poor. Fig. 2 *B* is a zero-loss electron image created with only
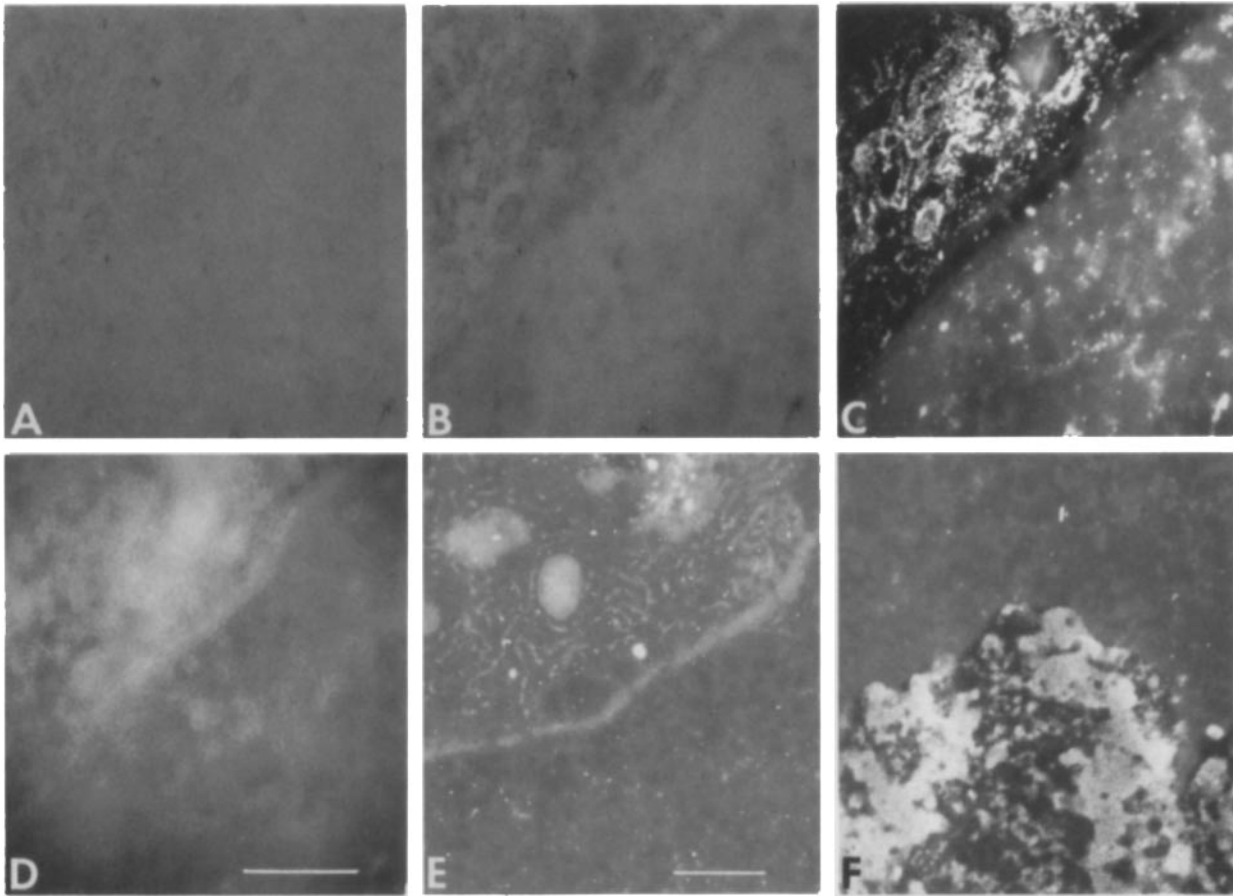
Figure 2. (*A–D*) A demonstration of changes in image contrast with different energy electrons. (*E* and *F*) Staining sensitivity of ribosomal and hnRNP, but not chromosomal DNA, to RNAse. (*A–D*) The same area of a Lowicryl section stained with OA-B and imaged with different energy loss electrons: *A*, global; *B*, $\Delta E = 0$; *C*, $\Delta E = 250$ eV; *D*, $\Delta E = 295$ eV. In *E* and *F*, Lowicryl sections were treated with RNase, followed by OA-B staining and imaged at 250 eV. The low contrast of OA-B–stained Lowicryl in the global imaging mode (using all electrons) is evident in *A*. Contrast is improved when zero-loss electrons are used in imaging (*B*). Note the high contrast of the tiny gold spheres. Biologic structures are more difficult to discern. At 250 eV loss (*C*), electrons scattered by the ubiquitous carbon atoms do not contribute to the image. Contrast is reversed and structures stained by OA-B are sharp and highly contrasted. The nuclear envelope follows a diagonal path from upper right to lower left, with cytoplasm in the upper left region and nucleoplasm in the lower right. The ribosomes in the cytoplasm dominate in stain intensity. RNP granules in the nucleoplasm and gold throughout the section are also evident. In *D* the strong carbon contribution makes it difficult to recognize any details. *E* and *F* of RNase-treated sections before OA-B staining demonstrate that removal of RNA reduces ribosomal and hnRNP contrast (*E*), but does not effect staining of banded polytene chromosomes (lower half of *F*). Bars: *A–D*, 500 nm; *E* and *F*, 1 μm.

elastically scattered electrons, and appears quite similar to the global image, but the contrast is slightly improved and shows more detail, especially for gold spheres. The sections are ∼75–150 nm in thickness; a thickness which prevents accurate elemental mapping. However, at different regions of the energy loss spectrum change in image contrast is a complicated function of elemental localization and mass-density effects. The sections are sufficiently thin so that most of the electrons do not suffer inelastic collisions with the specimen. Additional images taken at $\Delta E = 30$ eV and $\Delta E = 50$ eV had very little contrast and lacked structural detail. At $\Delta E = 100$ eV (osmium O_1 edge is at 84 eV) the contrast was reversed and stronger, but detail was not easily discerned. At $\Delta E = 160$ eV (phosphorus $L_{2,3}$ edge maximum is at 160 eV) contrast of presumptive RNA was stronger than for gold spheres. The images between $\Delta E = 30$ eV and $\Delta E = 160$ eV are not shown. The contrast and clarity of the image are especially

good at $\Delta E = 250$ eV (Fig. 2 *C*). Beyond the carbon K edge, however, an image recorded at $\Delta E = 295$ eV (Fig. 2 *D*) reveals a marked deterioration of contrast, since a high proportion of inelastically scattered electrons arise from background carbon. A more complete discussion of these contrast reversals with varying eV-loss windows has been presented (30). An electron energy-loss spectrum of an OA-B–stained specimen (Fig. 3) documents the sharp rise of inelastically scattered electrons occurring above $\Delta E = 275$ eV. The present data illustrates that structure-sensitive contrast enhancement can be performed with OA-B–stained sections.

Stereo EM Demonstrates Different Views of BR Granule Substructure

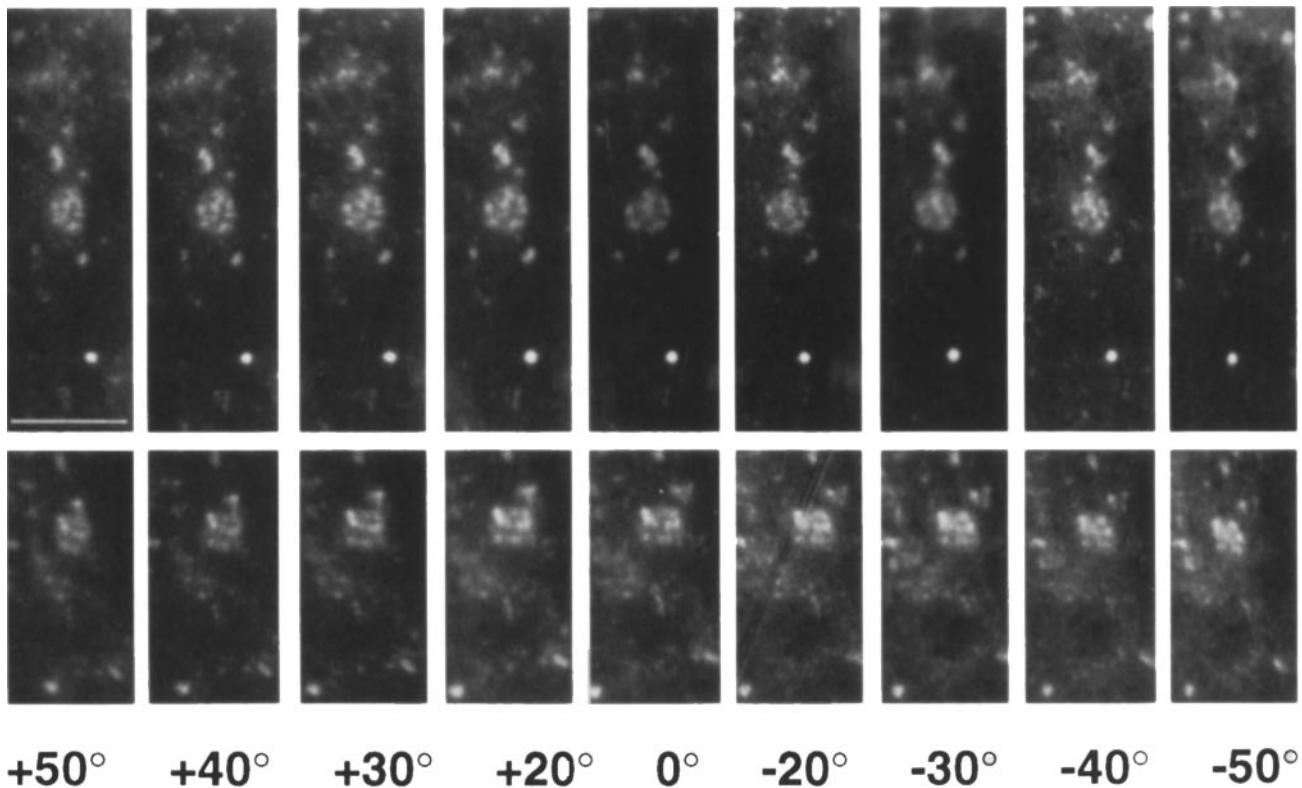Stereo pairs of individual mature BR granules were collected at 50 and 85K magnification to study the RNP substructure
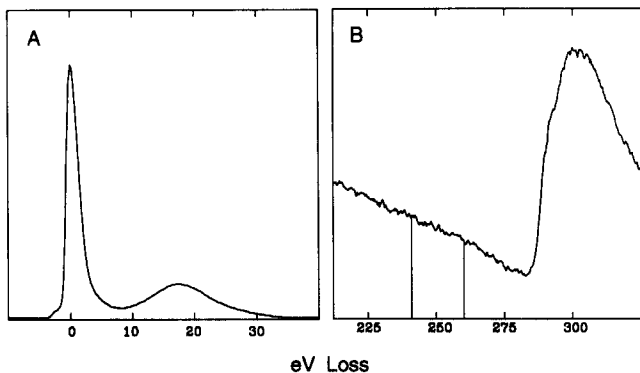
Figure 3. Two portions of the energy loss spectrum indicate that: (A) most of the electrons pass through the specimen without loss of energy ($\Delta E = 0$); and (B) the region of the spectrum used for most of the images ($\Delta E = 250 \pm 10$ eV) has a low intensity and precedes the large carbon K-edge at $\Delta E = 285$ eV. The y-axis (intensity) is magnified 650-fold in *B*, compared to *A*.

(Fig. 4). The RNA distribution is obviously not homogeneous, rather, the clearly punctate pattern of stain suggests segregation of RNA-rich and of protein-rich domains. Here we note that different perspectives, determined by the angle of sectioning, suggest the coiling of a string of hnRNP particles. This interpretation of the data is most clearly demonstrated in Fig. 5 where views of BR granules from two tilt series are presented at $\sim 10°$ intervals. If a stereo viewer is used the rotation of the BR granules is easily observed. The top tilt series appears to rotate around the "pin-wheel" orientation of a BR granule. Due to the specificity of the stain, the presumptive RNA is easily visualized without interference from the many proteinaceous structures in the nucleoplasm, even at very high tilt angles. The bottom series resembles rotation around an "edge-on" view of a short helix. From numerous measurements of OA-B stained BR granules, we obtain the following average parameters: BR granule outer diameter, 43.6 ± 0.6 nm (SEM), $n = 89$; particle diameter, 9.3 ± 0.1 nm (SEM), $n = 166$. By contrast, the aver-
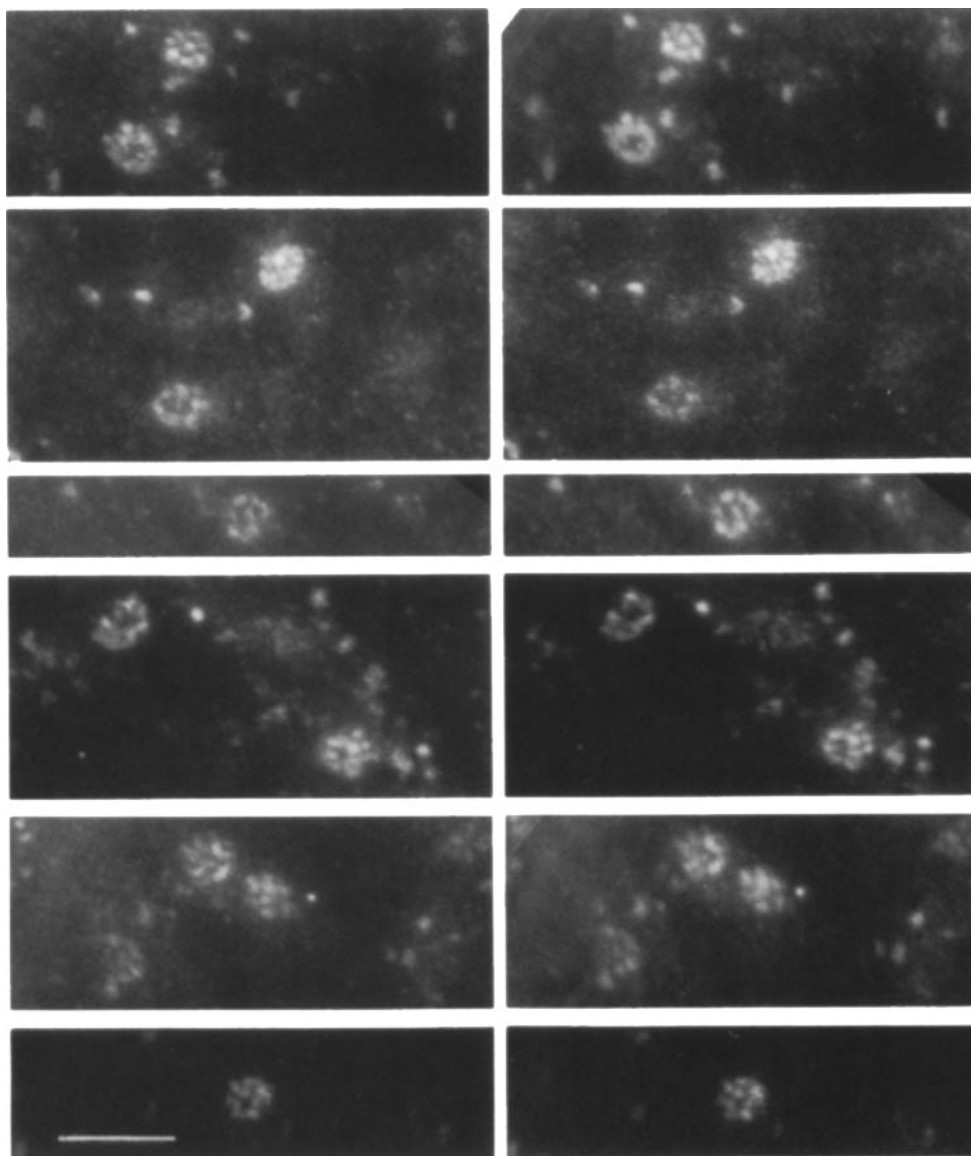
Figure 4. High magnification stereo EM pairs of mature BR granules demonstrate the organization of the RNA substructure from various perspectives. Notice the different orientations ranging from en face "pinwheel" structure to tilted views. Bar, 100 nm.

+50° +40° +30° +20° 0° -20° -30° -40° -50°

Figure 5. Representative projections of two tilt series of individual BR granules present a dynamic impression of the particulate substructure by moving a stereo viewer across the page. In this figure, BR granules can be observed as they tilt from +50° to −50°. The en face "pinwheel" view is evident in the top series. The bottom panel resembles an "edge-on" view of a short left-handed helix. Bar, 100 nm.

age diameter of cytoplasmic ribosomes (combining together measurements of long and short axes) was: 17.7 ± 0.5 nm (SEM), $n = 65$. It is difficult to estimate accurately the number of particles per BR granule. Careful study of many stereo images suggests that up to 10–12 particles can sometimes be observed; most BR granules appear to have less. At present, we assume that the lower numbers could arise for several reasons: (*a*) overlap of discrete particles in the images; (*b*) fusion or proximity of adjacent particles below the resolution of our methods; and (*c*) removal of some particles during sectioning. There may also be more than one type of BR granule substructure; BR1, 2, and 6 transcribe 35–40-kb mRNA (7, 10). Granules of similar outer diameter but distinctly fibrous substructure can also be readily identified within the nucleoplasm. None-the-less, the morphology of the BR granules with particulate substructure was so distinctive, and the proportion so great, that this class could be easily studied.

BR Granule Substructure Is Retained during Passage through Nuclear Pores

It is a simple matter to identify the nuclear envelope even though the OA-B stain does not exhibit significant binding to proteins and lipids; the high concentration of ribosomes in the cytoplasm ends abruptly at the edge of the unstructured nucleoplasm, defining the envelope (Fig. 2 *C*). A montage of stereo pairs of BR granules passing from the nucleoplasm on the left to the cytoplasm on the right is presented in Fig. 6. As visualized by OA-B staining, the unraveling BR granule

appears cone shaped with a leading string of particles passing through the nuclear envelope, whereas the uranyl- and lead-stained stereo pair (Fig. 6, bottom) appears more like a ribbon passing through the pore.

BR Granules Exhibit Phosphorus-rich Particles

To determine whether the OA-B was identifying an RNA-rich particle or whether the stain is only accessible by diffusion to certain domains of the granule, we obtained phosphorus-enhanced and net phosphorus images of BR granules. The granules were imaged in unstained thin sections (∼30-nm thick) of tissue. Both the phosphorus-enhanced images and the net phosphorus images showed particulate structure (Fig. 7). Since the sections are thinner than BR granule diameters (40–50 nm), only portions of granules were visible. The pattern obtained with the OA-B stain and the phosphorus maps of unstained specimens suggests that the RNA is localized in discrete domains within the BR granules.

Discussion

The present study demonstrates that a reproducible higher-order substructure of nascent and mature BR granule RNA is observed by a combination of selective nucleic acid staining and electron spectroscopic imaging (ESI) to enhance specimen contrast. This combination of methods holds considerable promise for the study of many DNA- and RNA-containing cellular structures. Combined with EMT (19,
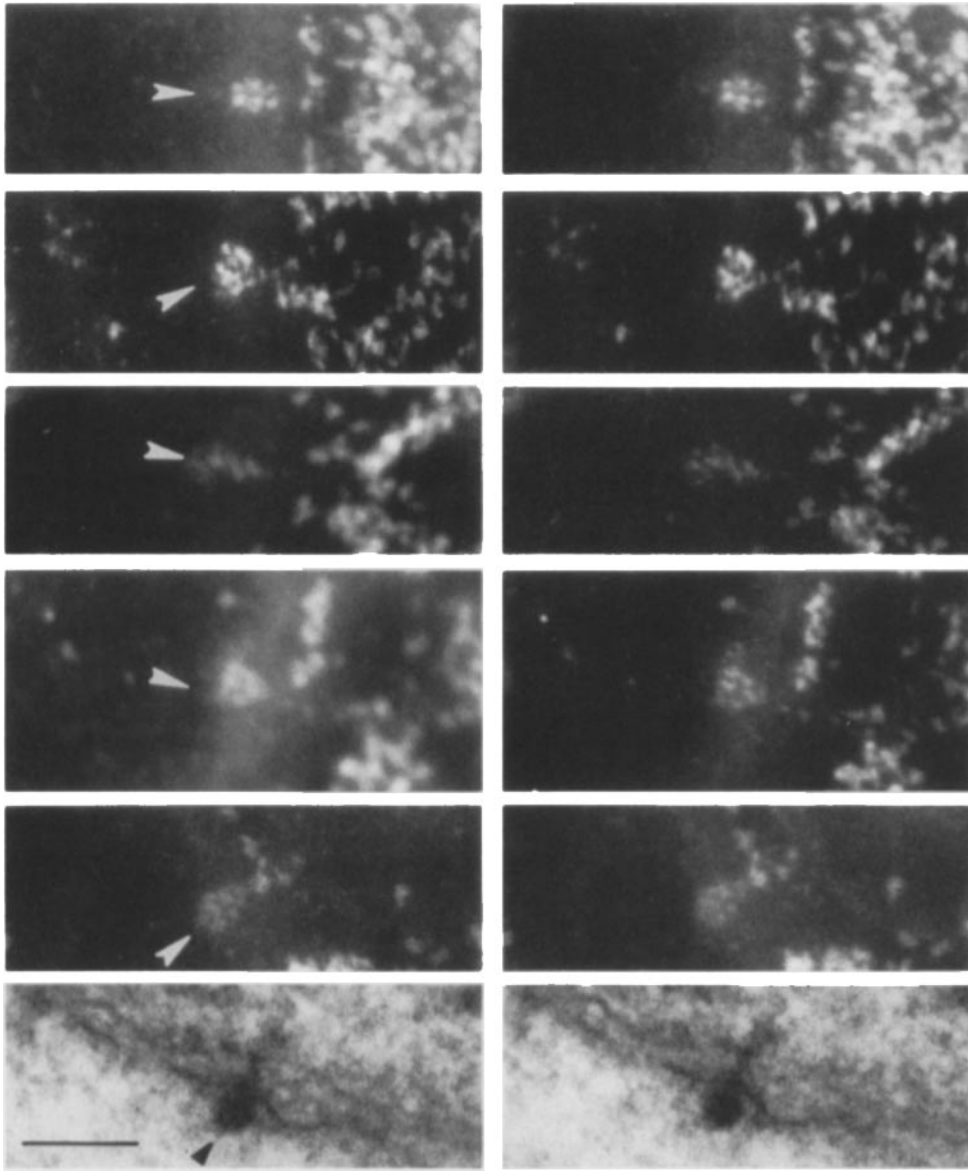
Figure 6. The BR granule as it passes through the nuclear envelope can be observed in this montage of stereo EM pairs. The cytoplasm is at the right, the nucleoplasm at the left (compare with Fig. 2 *C*). Arrowheads point the presumed direction of BR granule movement. A short string of 10-nm particles can often be observed leading the hnRNP into the cytoplasm. The bottom stereo pair was stained with uranyl and lead, contrasting lipids, proteins and nucleic acids. This image is representative of many published micrographs which demonstrate the elongation of the BR granule into a ribbon-like structure as it passes through the nuclear pore (20, 33). Bar, 100 nm.

24–26, 28, 33, 35, 38), it should be possible to develop more precise spatial models of the position and arrangement of subunits in these higher-order structures. EMT studies on BR granules are currently in progress.

Based upon extensive study of stereo images of OA-B–stained mature BR granules, we estimate that each granule contains 10–12 RNA-rich particles, with an average particle diameter of 9–10 nm. Dividing the total hnRNA length (∼37 kb) by 10–12 particles, yields 3.1–3.7-kb RNA per particle. The stereo images suggest that the particles are arranged into regular higher-order structures (e.g., "pinwheel" views are frequently observed; see Figs. 4 and 5). This higher-order packing appears to be disrupted when BR granules pass through nuclear pores; during transit the BR granule appears to unravel into a string of particles.

This study raises two significant questions: (*a*) Is there on obvious relationship between the 10-nm RNA-rich particles observed here in BR granules and the properties of ribonucleosomes (1, 8, 9, 13, 14)? and (*b*) How can this particulate

view of the BR granule be reconciled with the coiled ribbon model (19, 33, 35, 38)? Ribonucleosomes can be obtained as single 40S particles following extraction of RNAse-digested nuclei or RNAse treatment of reconstituted RNPs. These monomer particles consist of core proteins (30–40 kD) associated with 700 nucleotides at a protein/RNA weight ratio of 60/40, and exhibiting an overall diameter of ca. 20 nm. It is obvious that differences exist between isolated monomer ribonucleosomes and the BR granule particles; i.e., differences in the measured particle diameters and the estimates of associated RNA lengths. The discrepancy in particle diameters could be due to the fact that OA-B is staining RNA and not associated proteins. If we assume that the BR mRNA (37 kb) is covered with ribonucleosomes, we would estimate about 50 particles. The calculated volume of this number of ribonucleosomes would greatly exceed the volume of a BR granule. Furthermore, RNAse digestion of isolated BR granules did not yield convincing evidence for the existence of ribonucleosome subunits associated with the mRNA (39). In
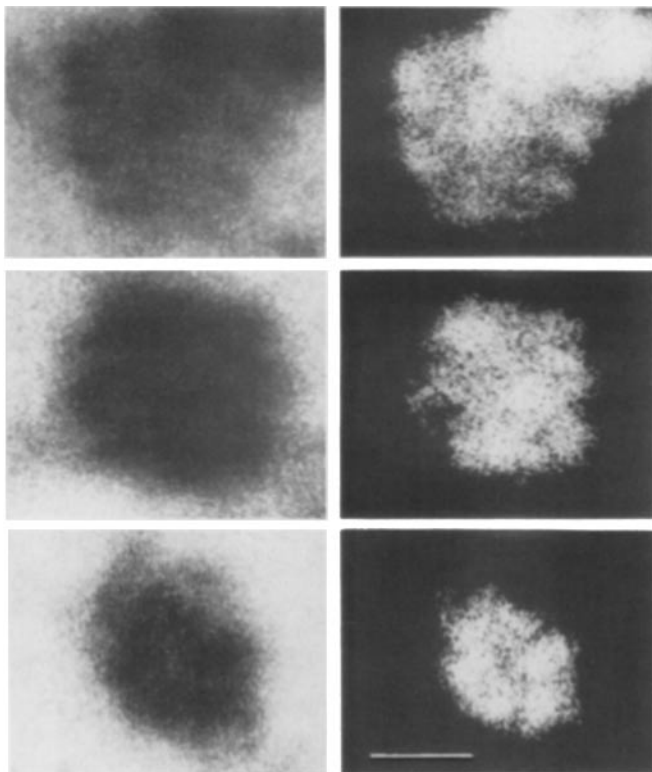
Figure 7. Net phosphorus distribution maps of three BR granules are shown on the right. These were obtained by subtraction of two images of the same area of very thin unstained lowicryl sections formed at two eV loss windows: $\Delta E = 120$ eV, the pre-edge image (not shown); $\Delta E = 160$ eV, the phosphorus enhanced image (*left*). The top granule gives a "pinwheel" appearance; the middle granule resembles an "edge-on" view. The bottom granule exhibits clear 10-nm particulate structures; but, the overall diameter is <40–50 nm, perhaps because of the removal of material during sectioning. Bar, 20 nm.

view of the evolutionary conservation of the hnRNP core proteins (8), it is likely that these proteins are associated with mRNAs in Chironomus. It must be concluded, however, that current evidence does not convincingly argue that the 10-nm particles are identical to ribonucleosomes. Could these BR granule substructures be spliceosomes? So far only a single 55-bp intron near the 3' end of the BR mRNA has been identified (7, 33), although the sequence for at least 75% of the coding region is known. The BR genes appear to contain U1 and U2 small nuclear RNP antigenic determinants within the puffs during transcription (32). However, mature BR granules appear to be unreactive to anti-small nuclear RNP antibodies (37), arguing against an identity between the 10-nm particles and mRNA splicing complexes. At present, the basis for the particulate appearance of BR granules remains unknown. It is possible that these structures are unique to BR genes. In an effort to answer this question, we have begun an examination of other genes that synthesize very large mRNAs.

EM studies of transcribing BR genes and mature BR granules have resulted in a coiled ribbon model for the large hnRNP (19, 33, 35, 38). Since these sections of nuclei were stained with uranyl acetate and lead citrate, the reconstructions would not distinguish between RNA- and protein-rich regions of the BR granule. The structure proposed is a ribbon ($\sim$120-nm long $\times$ 25–50-nm wide $\times$ 10–15-nm thick) bent into a ring. The authors argue that the 5' and 3' ends of the mRNA are in close proximity in the ring, separated by a barely discernable cleft. Further, it was suggested that the ring is somewhat skewed, suggesting a left handedness. Our image data focus attention upon the particulate character of the BR granule RNA and provide very little data on their connectivity. One provocative set of images is the tilt series of an apparent "edge-on" view of a single BR granule (Fig. 5, bottom series). This granule resembles a short left-handed
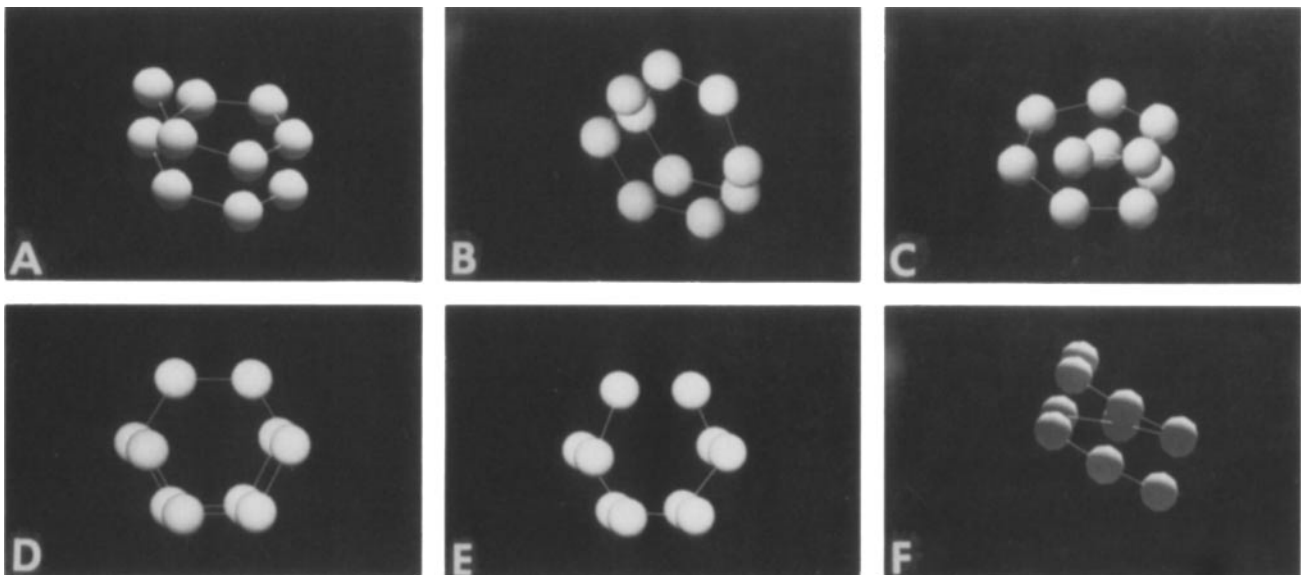
Figure 8. Various EM views of BR granule substructure are modeled by a shaded surface representation. This model consists of 10 particles connected in a single left-handed helix (10-nm-diam particles; six particles per turn; rotation angle 60°; 1 2/3 turns; rise per turn 15 nm). This figure is intended to simulate some of the images observed by EM, assuming a defined arrangement of particles, viewed at various orientations. Since the thin connections between particles are difficult to visualize, one can postulate a single helix (*A–D*, and *F*) or a zigzag connection (*E*). *A* simulates the "edge-on" view shown in the lower panel of Fig. 5. *B* and *C* simulate "pinwheel" views. *D* and *E* illustrate "en face" views. *F* simulates the top panel of our Fig. 6. More complicated models can be generated assuming more particles, and irregular spacings and connections.

helix. (We mount our stereo images based on "calibration" with a specimen of known handedness.) At least two types of models can be formulated in connecting the ~10-nm particles: (a) A single helical string 200–300-nm long, containing 10–12 particles; or (b) more complex connections, such as a "zig-zag" pattern between particles (Fig. 8). The nature of the arrangement of the 10-nm RNP particles and the order of their connections within the entire protein and RNA volume of the BR granules requires more analysis. Three-dimensional reconstruction data by EMT may permit such a comparison, leading to the formulation of more definitive models.

References

1. Barnett, S. F., T. A. Theiry, and W. M. LeStourgeon. 1991. The core proteins A2 and B1 exist as (A2)₃ B1 tetramers in 40S nuclear ribonucleoprotein particles. *Mol. Cell. Biol.* 11:864–871.
2. Bauer, R., V. Hezel, and D. Kurz. 1987. High-resolution imagining of thick biological specimens with an imaging energy loss spectrometer. *Optik.* 77:171–174.
3. Bazett-Jones, D. P. 1988. Phosphorus imaging of the 7-S ribonucleoprotein particle. *J. Ultrastruct. Mol. Struct. Res.* 99:59–69.
4. Bazett-Jones, D. P., and F. P. Ottensmeyer. 1981. Phosphorus distribution in the nucleosome. *Science (Wash. DC).* 211:169–170.
5. Bazett-Jones, D. P., L. Locklear, and J. B. Rattner. 1988. Electron spectroscopic imaging of DNA. *J. Ultrastruct. Mol. Struct. Res.* 99:48–58.
6. Beermann, W., and G. F. Bahr. 1954. The submicroscopic structure of the Balbiani Ring. *Exp. Cell. Res.* 6:195–201.
7. Botella, L. M., and J.-E. Edström. 1991. The Balbiani Ring 6 induction in chironomus. *Biol. Cell.* 71:11–16.
8. Chung, S. Y., and J. Wooley. 1986. Set of novel, conserved proteins fold pre-messenger RNA into ribonucleosomes. *Proteins: Struct. Funct. Genet.* 1:195–210.
9. Conway, G., J. Wooley, T. Bibring, and W. M. LeStourgeon. 1988. Ribonucleoproteins package 700 nucleotides of pre-mRNA into a repeating array of regular particles. *Mol. Cell Biol.* 8:2884–2895.
10. Daneholt, B. 1982. Structural and functional analysis of Balbiani Ring genes in the salivary glands of chironomus tentans. *In* Insect Ultrastructure. R. King and H. Akai, editors. Plenum Publishing Corp., New York. 1:382–401.
11. Derenzini, M., and F. Farabegoli. 1990. Selective staining of nucleic acids by osmium-ammine complex in thin sections from lowicryl-embedded samples. *J. Histochem. Cytochem.* 38:1495–1501.
12. Derenzini, M., D. Hernandez-Verdun, and M. Bouteille. 1983. Structure of a repeating subunit organization in rat hepatocyte chromatin fixed in situ. *J. Cell Sci.* 61:137–149.
13. Dreyfuss, G., L. Philipson, and I. W. Mattaj. 1988. Ribonucleoprotein particles in cellular processes. *J. Cell Biol.* 106:1419–1425.
14. Dreyfuss, G., M. S. Swanson, and S. Pinol-Roma. 1988. Heterogeneous nuclear ribonucleoprotein particles and the pathway of mRNA formation. *Trends Biochem. Sci.* 13:86–91.

15. Deleted in proof.
16. Gautier, A. 1976. Ultrastructural localization of DNA in ultrathin tissue sections. *Int. Rev. Cytol.* 44:113–191.
17. Ineichen, H., B. Meyer, and M. Lezzi. 1983. Determination of the developmental stage of living fourth instar larvae of chironomus tentans. *Dev. Biol.* 98:278–286.
18. Kim, S.-H., B. A. Moyer, S. Azan, G. M. Brown, A. L. Olins, and D. P. Allison. 1989. Preparation and properties of the nitrido-bridged osmium (IV) binuclear complexes [Os$^{IV}_2$N(NH$_{310-n}$Cl$_n$]Cl$_{5-n}$(n = 2,3). *Inorg. Chem.* 28:4648–4650.
19. Mehlin, H., A. Lonnroth, U. Sköglund, and B. Daneholt. 1988. Structure and transport of a specific premessenger RNP particle. *Cell Biol. Int. Reports.* 12:729–736.
20. Mehlin, H., U. Sköglund, and B. Daneholt. 1991. Transport of Balbiani Ring granules through nuclear pores in chironomus tentans. *Exp. Cell Res.* 193:72–77.
21. Meyer, B., R. Mahr, M. Eppenberger, and M. Lezzi. 1983. The activity of Balbiani Rings 1 and 2 in salivary glands of chironomus tentans larvae under different modes of development and pilocarpine treatment. *Dev. Biol.* 98:265–277.
22. Olins, A. L., D. E. Olins, and W. W. Franke. 1980. Stereo-electron microscopy of nucleoli, Balbiani Rings and endoplasmic reticulum in chironomus salivary gland cells. *Eur. J. Cell Biol.* 22:714–723.
23. Olins, A. L., D. E. Olins, and M. Lezzi. 1982. Ultrastructural studies of chironomus salivary gland cells in different states of Balbiani Ring activity. *Eur. J. Cell Biol.* 27:161–169.
24. Olins, D. E., A. L. Olins, H. A. Levy, R. C. Durfee, S. M. Margle, E. P. Tinnel, and S. D. Dover. 1983. Electron microscope tomography: transcription in three dimensions. *Science (Wash. DC).* 220:498–500.
25. Olins, A. L., D. E. Olins, H. A. Levy, R. C. Durfee, S. M. Margle, E. P. Tinnel, B. E. Hingerty, S. D. Dover, and H. Fuchs. 1984. Modeling Balbiani Ring gene transcription with electron microscope tomography. *Eur. J. Cell Biol.* 35:129–142.
26. Olins, A. L., D. E. Olins, H. A. Levy, R. C. Durfee, S. M. Margle, and E. P. Tinnel. 1986. DNA compaction during intense transcription measured by electron microscope tomography. *Eur. J. Cell Biol.* 40:105–110.
27. Olins, A. L., B. A. Moyer, S.-H. Kim, and D. P. Allison. 1989. Synthesis of a more stable osmium ammine electron-dense DNA stain. *J. Histochem. Cytochem.* 37:395–398.
28. Olins, A. L., D. E. Olins, H. A. Levy, S. M. Margle, E. P. Tinnel, and R. C. Durfee. 1989. Tomographic reconstruction from energy-filtered images of thick biological sections. *J. Microsc.* 154:257–265.
29. Rattner, J. B., and D. P. Bazett-Jones. 1989. Kinetochore structure: electron spectroscopic imaging of the kinetochore. *J. Cell Biol.* 108:1209–1219.
30. Reimer, L., I. Fromm, and R. Rennekamp. 1987. Operation modes of electron spectroscopic imaging and electron energy-loss spectroscopy in a transmission electron microscope. *Ultramicrosc.* 24:339–354.
31. Reimer, L., and M. Ross-Messemer. 1989. Contrast in the electron spectroscopic imaging mode of a TEM. II. Z-Ratio, structure-sensitive and phase contrast. *J. Microsc.* 159:143–160.
32. Sass, H., and T. Pederson. 1984. Transcription-dependent localization of U1 and U2 small nuclear ribonucleoproteins at major sites of gene activity in polytene chromosomes. *J. Mol. Biol.* 180:911–926.
33. Sköglund, U., and B. Daneholt. 1986. Electron Microscope Tomography. *Trends Biochem. Sci.* 11:499–503.
33a. Silva, F. J., L. M. Botella, and J.-E. Edström. 1990. Functional analysis of the 3'-terminal part of the Balbiani Ring 2.2 gene by interspecies sequence comparison. *J. Mol. Evol.* 31:221–227.
34. Sköglund, M., K. Anderson, B. Bjorkroth, M. M. Lamb, and B. Daneholt. 1983. Visualization of the formation and transport of a specific hnRNP particle. *Cell.* 34:847–855.
35. Sköglund, U., K. Andersson, B. Strandberg, and B. Daneholt. 1986. Three-dimensional structure of a specific pre-messenger RNP established by electron microscope tomography. *Nature (Lond.).* 319:560–564.
36. Stevens, B. J., and H. Swift. 1966. RNA transport from nucleus to cytoplasm in chironomus salivary glands. *J. Cell Biol.* 31:55–77.
37. Vazquez, G. H., O. M. Echeverria, S. Fakan, G. Leser, and T. E. Martin. 1990. Immunoelectron microscope localization of snRNPs in the polytene nucleus of salivary glands of Chironomus thummi. *Chromosoma.* 99:44–51.
38. Wurtz, T., A. Lonnroth, L. Ovchinnikov, U. Sköglund, and B. Daneholt. 1990. Isolation and initial characterization of a specific premessenger ribonucleoprotein particle. *Proc. Natl. Acad. Sci. USA.* 87:831–835.
39. Wurtz, T., A. Lonnroth, and B. Daneholt. 1990. Higher order structure of Balbiani Ring premessenger RNP particles depends on certain RNAse A sensitive sites. *J. Mol. Biol.* 215:93–101.